

Article

Studying the Effects of Wave Dissipation Structure and Multiple Size Diffusion Chambers on Explosion Shock Wave Propagation

Wei Liu ¹, Xiangyun Xu ^{2,*}, Huahui Yi ^{3,*} and Lifan Zhu ⁴

¹ Institute of Engineering Safety and Disaster Prevention, Hohai University, Nanjing 210098, China; wliu916@163.com

² Institute of Defense Engineering, PLA Academy of Military Science, Beijing 100080, China

³ School of Weapon Science and Technology, Xi'an Technological University, Xi'an 710021, China

⁴ State Key Laboratory of Mining Response and Disaster Prevention and Control in Deep Coal Mines, Anhui University of Science and Technology, Huainan 232001, China; ac777hz5@126.com

* Correspondence: pla53294323@126.com (X.X.); llh5428879@163.com (H.Y.); Tel.: +86-18467051925 (X.X.)

Abstract: Explosion chambers are crucial to the technology used to prevent coal mine gas explosions. Investigating the shock wave propagation law at various coal mine tunnel cross-sections helps ensure mine safety. A self-built, highly explosive experimental setup was used to conduct empirical research on straight tubes, eight sizes of single-stage explosion chambers, and multi-stage tandem explosion chambers. Ansys Fluent numerical simulation software constructed five different tandem explosion chamber models. The wave dissipation efficiency of various types of explosion chambers was calculated, the propagation law and process of shock waves across multiple explosion chambers were examined, and the best size and type of explosion chambers were summarized to increase the wave dissipation efficiency of single-stage explosion chambers. Gun silencers inspired these models. The findings indicate that the three-stage tandem explosion chamber is the best diffusion tandem combination form, the 60° silencer-type explosion chamber is the best single-stage explosion chamber modification program, and the 500 mm × 500 mm × 200 mm explosion chamber is the best single-stage explosion chamber.

Keywords: explosion chamber; wave-absorbing structure; explosion shock wave; explosion suppression



Citation: Liu, W.; Xu, X.; Yi, H.; Zhu, L. Studying the Effects of Wave Dissipation Structure and Multiple Size Diffusion Chambers on Explosion Shock Wave Propagation. *Fire* **2023**, *6*, 371. <https://doi.org/10.3390/fire6100371>

Academic Editors: Hengrui Liu and Anthony Chun Yin Yuen

Received: 30 August 2023

Revised: 17 September 2023

Accepted: 18 September 2023

Published: 24 September 2023



Copyright: © 2023 by the authors. Licensee MDPI, Basel, Switzerland. This article is an open access article distributed under the terms and conditions of the Creative Commons Attribution (CC BY) license (<https://creativecommons.org/licenses/by/4.0/>).

1. Introduction

Gas explosion shock waves in coal mine tunnels significantly harm workers and mining equipment [1–3]. The gas explosion shock wave suppression technology used in coal mines has relied chiefly on explosion-proof rock powder and explosion-proof water bags for a very long period. The explosion-proof rock powder sheds and the water sheets are one-time solutions that cannot withstand repeated explosions. Recently, we've created a diffusion chamber wave attenuation technique [4,5]. We continue to call it an “explosion chamber” since the varied cross-sections of coal mine tunnels are comparable to the structure used in civil air defense engineering. It is challenging to renovate the existing explosion chamber due to the constrained subterranean area in coal mines. To ensure coal mine safety, it is essential to investigate the explosion chamber's ideal size design and suitable structural shape.

Nowadays, the following three categories serve as the primary divisions for the explosion chamber wave dissipation efficiency optimization design, with the first category adopting absorbent materials to absorb the blast shock wave energy. The second type is the dispersion of indoor-laying explosion suppression powder, which is accomplished by the explosion suppression powder physically and chemically absorbing the explosive shock wave energy. The third category, the active blast isolation device, which relies on advanced sensors to collect the explosion information to initiate the blast isolation system, is presently more common for usage in blast isolation devices to limit blast shock wave energy.

The first category focuses on wave-absorbing materials research. Through pendulum impact experiments and numerical simulations, Shi et al. [6] investigated the mechanical response of a human defense wall sprayed with POZD material. Iqbal et al.'s [7] experimental investigation of the mechanical behavior of polyurea-sprayed masonry walls under blast loads revealed that energy absorption improves with coating thickness and that polyurea composites with a thickness of 6 mm can tolerate higher pressures. By conducting this experiment, Grigory Bivol et al. [8] investigated the suppressing impact of polyurethane foam with various pore sizes on blast waves.

The second category, which relates to explosive suppression powder, is often broken down into solid explosive suppressants, liquid explosive suppressants, and gas explosive suppressants. The authors [9] investigated the effects of rock powder, water, and ABC dry powder on the explosion shock wave through experimental studies on solid explosive suppressants. Via a vertical combustion tube, Zhao et al. [10] examined the deflagration of methane, coal dust, and ABC dry powder. Through experimentation, Li et al. [11] analyzed the CO₂ and ultrafine ABC dry powder explosion suppression method. Through experimental quantification, Song et al. [12] investigated the impact of sedimentary rock powder volume on explosion overpressure, temperature, and flame velocity. Fan et al. [13] examined the NaHCO₃ fire extinguisher powder's explosion suppression mechanism using numerical calculations and experimentation. According to Liu et al.'s [14] investigation into the effects of spray pressure and temperature on water mist suppression, a water mist at 20 °C had the best result. Pei et al. [15] conducted N₂-biofluid acceptable water mist explosion suppression tests using a self-built experimental apparatus. In a numerical simulation study conducted by Cao et al. [16], the heat transfer process between an ultrafine water mist and the explosion flame and the mechanism of ultrafine water mist-induced explosion inhibition were examined. According to Lu et al.'s [17] experimental investigation of nitrogen's impact on blast shock wave suppression in horizontal pipes, 0.2 MPa of nitrogen may successfully halt the blast shock wave's propagation.

The third category, active and passive explosion-proof devices, are the two primary categories of explosion-proof equipment. With an active blast isolator, Jiang et al. [18] investigated the effects of nitrogen and ABC dry powder on blast suppression. Yang [19] used an active visualization experimental platform to confirm the inhibition effect of methane-oxidizing bacteria on blast shock waves. The study of good blast suppression structure knots on the development of new blast suppression technology and the improvement of the existing blast suppression technology is of great significance as the overall structure of the explosion chamber is not easily destroyed and can effectively resist multiple explosive shock waves.

Experimental research on eight single diffusion chamber sizes and four different series of diffusion chamber kinds confirmed the wave attenuation effect of series diffusion chambers. The propagation law and process of shock waves in various diffusion chambers were examined, and the ideal size and type of diffusion chamber were summarized. The wave attenuation effects of nine different types of diffusion chamber structures were verified through numerical simulation, and the wave attenuation efficiency of various types of diffusion chambers was calculated.

2. Program and System for Explosive Testing

2.1. Test Systems

A highly explosive experimental apparatus with a self-built pipe of 36,000 mm long and 200 mm in diameter was used. The testing system comprises the gas distribution, piping, igniting, and data-collecting subsystems. Figure 1a displays the practical system's schematic diagram, and Figure 1b shows the system's photographs. The pipe subsystem comprises a steel pipe with a 200 mm inner diameter and a 10 mm wall thickness that is separated into a detonation pipe, connecting pipe, and propagation pipe. The propagation tube is 20,000 mm long, the connection tube is 2000 mm, and the detonation tube is 11,000 mm long. The air compressor, vacuum pump, methane gas cylinder, circulation

pump, and electronic pressure gauge comprise the bulk of the gas distribution subsystem. The major components of the ignition subsystem are the electrode, power source, electric fuse, and ignition controller. Most of the data collection system members are pressure sensors, high-speed data-gathering equipment, and data processing software. For the trials, 99.9% pure high-quality methane gas was employed. The pressure sensor range is 0–3 MPa, the accuracy level is 0.5% FS, and the ignition energy may be up to 10 J. In the explosive tube, methane and air are combined, and a diaphragm cuts off the connecting line.

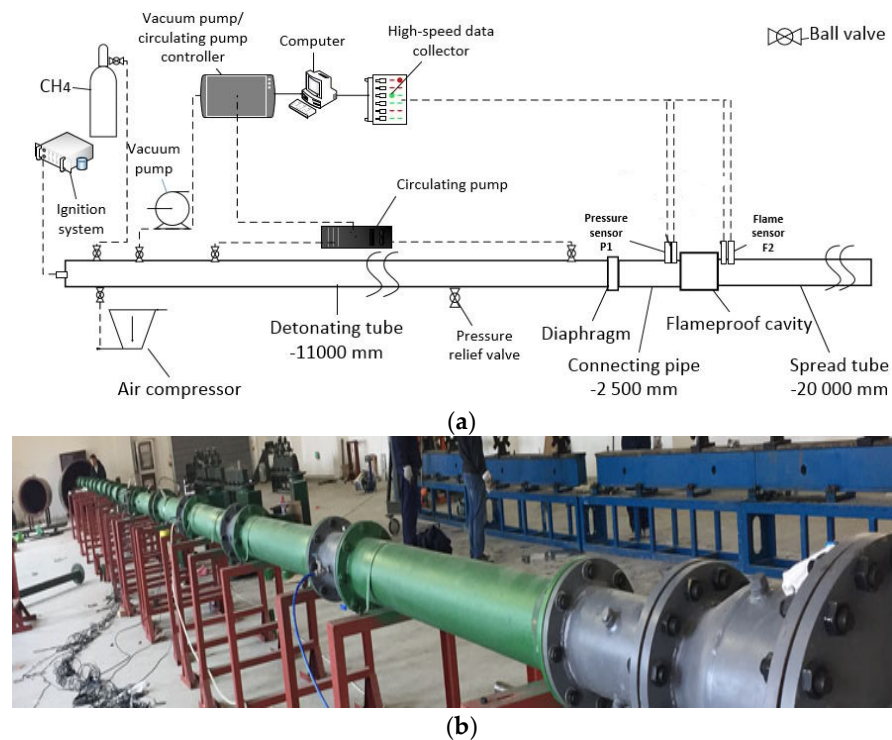


Figure 1. Physical and schematic representations of the experimental system.

The vastness of coal mine underground tunnels makes prototype experiments expensive and safety concerns prevalent. As a result, scaling experiments are widely used for researching gas explosions in coal mines [20], as demonstrated by this paper.

2.2. Test Systems

2.2.1. Program for Testing Straight Tubes and Single-Stage Explosion Chambers

The straight tube test is intended to be contrasted with the explosion chamber test, with the sensor's location remaining constant between the two tests.

According to the construction and support specifications, the explosion chamber's length and breadth should not exceed four times the roadway's diameter. As a result, the length, width, and height of this experiment were custom-made for explosion chambers in the following sizes: 300 mm × 300 mm × 200 mm (3–3), 300 mm × 500 mm × 200 mm (3–5), 300 mm × 800 mm × 200 mm (3–8), 500 mm × 300 mm × 200 mm (5–3), 500 mm × 500 mm × 200 mm (5–5), 800 mm × 300 mm × 200 mm (8–3), 800 mm × 500 mm × 200 mm (8–5), and eight other sizes. To increase the viability of the numerical simulations, experimental investigations were used to validate them, and based on these studies, more research was conducted. Figure 2 depicts the explosion chamber model's schematic diagram, while Figure 3 depicts the chamber.

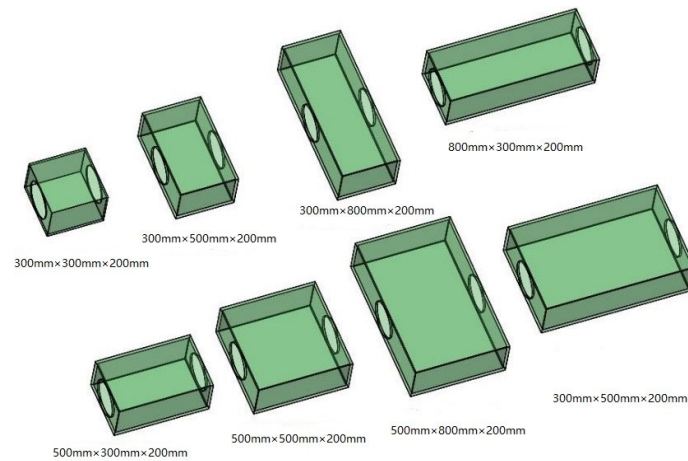


Figure 2. Schematic illustration of the explosion chamber model.



Figure 3. Physical model of the explosion chamber.

2.2.2. Test Procedure for a Multi-Stage Series Explosion Chamber

Existing research suggests that the explosion chamber construction may contribute in some way to eliminating shock waves. To increase the wave attenuation efficiency, we must undertake an experimental study on the wave attenuation impact of several explosion chambers in series. The series explosion chamber test is an exploratory test due to the constraints of the test environment. The restricted number of explosion chamber models led to the selection of various-sized explosion chamber combinations for experimental testing. The explosion chamber structures with dimensions of 500 mm × 500 mm × 200 mm and 500 mm × 800 mm × 200 mm have apparent effects on reducing the shock wave of a methane explosion, and 300 mm × 500 mm × 200 mm have sound effects on lowering the explosion flame velocity, according to the previous research findings of our research group [5]. As a result, experiments using multiple explosion chamber series 55–35 and 58–35–55 were carried out. Figure 4 displays the schematic design and images of the multi-stage series explosion chamber test.

2.2.3. Test Procedure

After the straight pipe methane explosion experiment, the eight explosion chambers were individually tested experimentally. The pressure sensors were mounted at the places indicated in Table 1 and labeled P1 and P2.

Table 1. Location of the pressure sensor.

Pressure Sensor	Placement of the Measuring Points
Pressure sensor P1	13.2 m
Pressure sensor P2	14.2 m

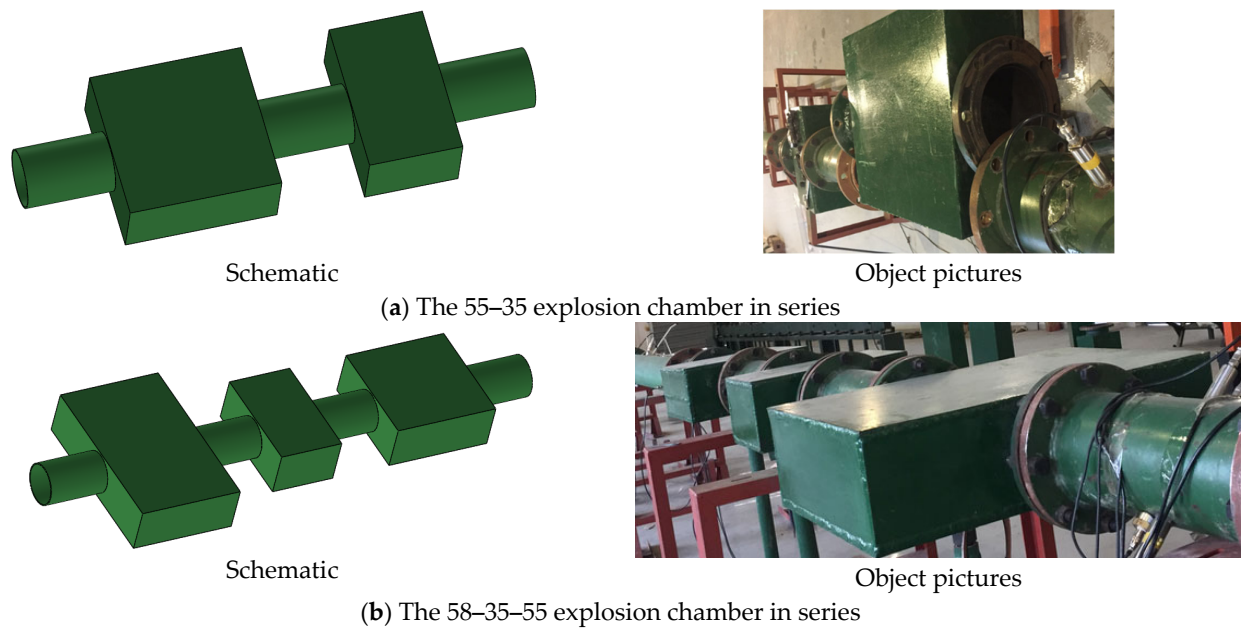


Figure 4. Multiple-stage series explosion chamber.

Setting up a pressure sensor before and after the diffusion chamber is necessary to track the variations in shock wave pressure. The variations in shock wave pressure before and after the diffusion chamber can then be used to assess the effectiveness of the diffusion chamber. When methane concentration reaches 9.5%, the explosive power is at its peak. As a result, a 9.5% methane concentration was chosen for this article. Below is the particular experimental protocol:

- (1) Initiate all test systems and commission all equipment for everyday use.
- (2) Put in the diaphragm, then gasket it.
- (3) Launch the gas distribution system and set the gas concentration to 9.5 percent.
- (4) Turn on the circulation pump, which will circulate the gas flow within the explosion chamber for 20 min to guarantee homogeneity.
- (5) Test the real-time collection mode of the collection system.
- (6) Make the ignition subsystem operational so that the ignition may work.
- (7) Preserve data.

3. Analyzing Numerical Simulations

3.1. Models in Geometry

3.1.1. Single-Stage Explosion Chamber Geometric Model

The indoor plane should be square or rectangular, and the diffusion chamber should be poured entirely with reinforced concrete. Currently, the diffusion chamber is primarily square. The 5–5 (500 mm × 500 mm × 200 mm) explosion chamber is the subject of investigation for experimental tandem numerical simulation in this work. Figure 5 depicts a 500 mm × 500 mm × 200 mm explosion chamber model.

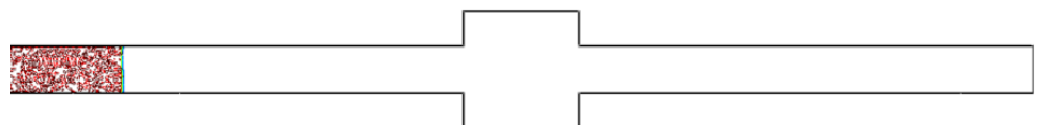


Figure 5. Model of a 500 mm × 500 mm × 200 mm explosion chamber.

3.1.2. Multi-Stage Tandem Explosion Chamber Geometric Model

Multi-stage explosion chambers were designed in sequence and based on the 5–5 (500 mm × 500 mm × 200 mm) explosion chamber, as illustrated in Figure 6. Tandem explosion chamber versions with two, three, four, and five stages each were constructed.

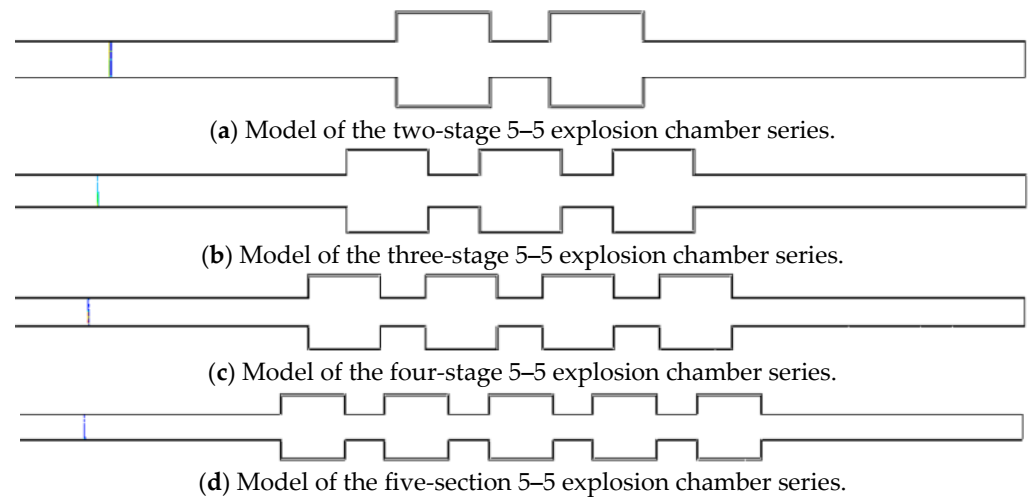


Figure 6. Model of the 5–5 multi-Stage explosion chamber series.

3.1.3. Silencer-Type Explosion Chamber Geometric Model

Existing human defense project space is constrained, making it challenging to build numerous explosion chambers, which means only current explosion chambers can be improved. To increase the protection potential of human defense projects, it is crucial to optimize the design of the wave dissipation impact of a single-stage explosion chamber and increase the wave dissipation capacity of a single-stage explosion chamber. Figure 7 depicts the gun's silencer construction. The wave elimination plate and the silencer structure's changing cross-section can potentially damper acoustic waves. As a result of quick pressure changes, shock waves are pulsed sound waves from an aerodynamic standpoint. Therefore, silencers are excellent at reducing sound waves. This paper attempts to construct a wave dissipation plate similar to the design of the silencer in the explosion chamber, drawing inspiration from the "silencer" structure of the gun. By varying the angle of the plate, it aims to determine the ideal angle of the wave dissipation effect, and thus make it easier to transform the explosion chamber currently used for the human defense project. Nine distinct explosion chamber models with wave elimination plate angles of 30°, 45°, 60°, 75°, 90°, 105°, 120°, 135°, and 150° were constructed; the angles are represented schematically in Figure 8 and the models are explained in Figure 9.



Figure 7. Silencer architecture.

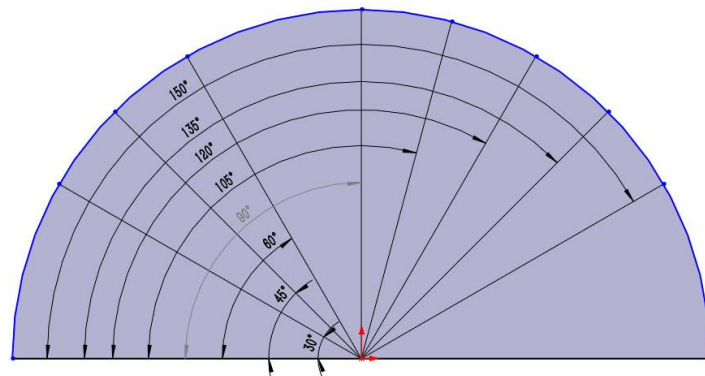


Figure 8. Angle diagram.

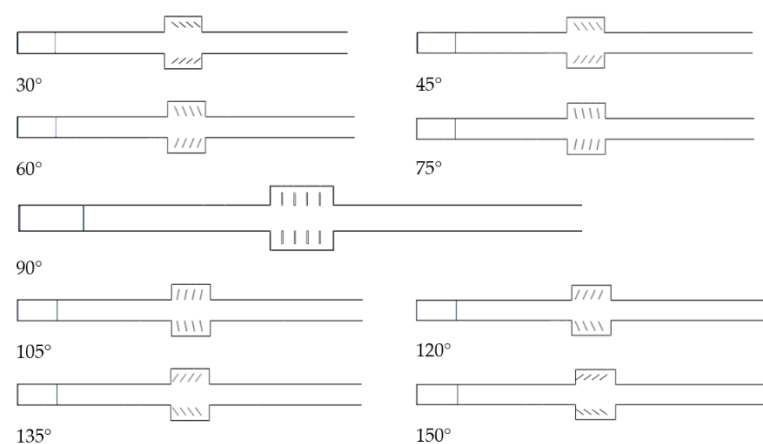


Figure 9. Wave attenuation structural model at various angles.

3.2. Models in Mathematics

Methane explosion is a quick and intricate process brought on by chemical reactions and turbulent motion. The numerical simulations were carried out with the following presumptions in mind:

- (1) Suppose that the methane explosion is a process of ideal gas expansion that has been heated;
- (2) Disregard the radiative exotherm of the blast shock wave during the propagation process and the flow–solid coupling effect between the inner wall and the shock wave by assuming that the pipe and explosion chamber walls are adiabatic and that no heat exchange occurs;
- (3) Assume that the methane is at rest before ignition, obeys Moore's law, and is well mixed with air when it bursts;
- (4) Suppose the Mach bar is a plane surge parallel to the inside wall.

The reaction is the most complete when the volume percentage of methane in the air reaches 9.5. As a result, 9.5% of the volume of the methane–air premixed gas chosen for the numerical simulation contains methane. This work uses a two-step reaction model with high accuracy, and this model has the properties of high precision and high reliability to increase the reliability and accuracy of the simulation results. The reaction process is as follows:



(1) An equation for the combustion reaction

The model’s characteristics for the methane–air response are the volumetric reaction, rigid chemical solver, diffusion energy source, complete multicomponent diffusion, and thermal diffusion. Here is the Arrhenius rate equation:

$$k = AT^b \exp\left(-\frac{E_a}{RT}\right), \tag{3}$$

where T is the absolute temperature; b is the temperature index; A is the pre-exponential factor, $\text{mol}/(\text{m}^3 \cdot \text{s})$; k is the response rate parameter, $\text{mol}/(\text{m}^3 \cdot \text{s})$; the reaction activation energy is known as E_a , J/mol ; the molar gas constant is R , $8.3144 \text{ J}/(\text{mol} \cdot \text{K})$.

(2) Energy equation

$$\begin{aligned} \frac{\partial}{\partial t}(\rho E) + \nabla \left[\vec{u}(\rho E + p) \right] &= \nabla \left[k_{eff} \nabla T - \sum_j h_j J_j + (k_{eff} \cdot \vec{u}) \right] + S_h + \vec{Q} \\ E &= h - \frac{p}{\rho} + \frac{u^2}{2} \\ h_j &= \int_{T_{ref}}^T C_{p,j} dT \\ k_{eff} &= k + k_t \end{aligned}, \tag{4}$$

where E indicates the total energy of the fluid, which is the sum of internal energy, kinetic energy, and potential energy, J/kg ; h stands for enthalpy, J/kg ; $k_{eff} = 298.15\text{K}$; h_j is enthalpy of component j , J/kg ; J_j is the diffusion flux of component j , K_{eff} is the effective thermal conductivity coefficient, $\text{W}/(\text{m} \cdot \text{K})$, k_t is the turbulent thermal conductivity coefficient, $\text{W}/(\text{m} \cdot \text{K})$; S_h stands for the volumetric heat source term, and Q for the exchange of mass, momentum, and energy between the liquid droplet and the continuous gas phase.

(3) $k-\varepsilon$ equation

$$\rho \frac{dk}{dt} = \frac{\partial}{\partial x_i} \left[\left(u + \frac{u_t}{\sigma_k} \right) \right] + G_k + G_b - \rho \varepsilon - Y_M, \tag{5}$$

$$\rho \frac{d\varepsilon}{dt} = \left[\left(u + \frac{u_t}{\sigma_k} \right) \frac{\partial k}{\partial x_i} \right] + C_{1\varepsilon} \frac{\varepsilon}{k} (G_k + C_{3\varepsilon} G_b) - C_{2\varepsilon} \rho \frac{\varepsilon^2}{k}, \tag{6}$$

where Y_M is the fluctuation caused by the diffusion of the compressible turbulent transition, J ; G_k is the turbulent kinetic energy owing to the laminar velocity gradient, J ; G_b is the turbulent kinetic energy related to the buoyancy effect, J .

3.3. Dividing a Grid

The sparsity of the mesh division impacts whether the explosion shock wave front can be correctly captured since the methane explosion itself is a quick reaction process. The numerical model in this article features a finer mesh division of the explosion chamber structure in order to more properly represent the shock wave propagation mechanism in the explosion chamber. Grid units are 0.05 m in the explosion chamber and 0.005 m elsewhere. Figure 10 depicts the schematic grid division diagram.

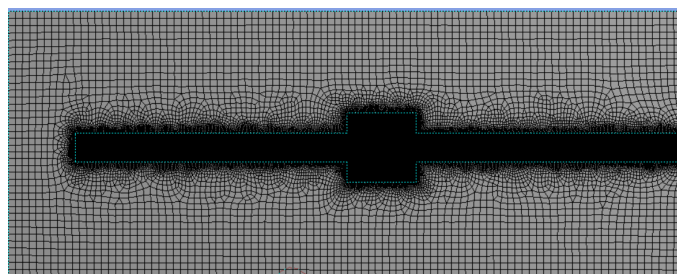


Figure 10. Schematic grid divider diagram.

3.4. Initial Circumstances, Boundary Conditions, and Monitoring Points

This study uses the finite volume method, which partitions the computational space into several dispersed finite control volumes. We ensure that a limited control volume surrounds each grid point, and we integrate the parameters needed to solve the differential equations for each finite control volume to produce a set of discrete equations.

This study uses the finite volume method, which partitions the computational space into several dispersed limited control volumes. We ensure that a finite control volume surrounds each grid point, and we integrate the parameters needed to solve the differential equations for each small control volume to produce a set of discrete equations. Steger–Warming is utilized to create the physical quantities in differential formats; the WENO format is used for discretization in the spatial dimension; and the LU-SSOR approach is used for discretization in the temporal dimension. The beginning conditions are the gas combination’s pressure, temperature, and velocity. The walls of the pipe and cavity are adiabatic, and no-slip is present. We set the monitoring points at 200 mm before and after the explosion chamber because the peak overpressure before and after the explosion chamber is a crucial criterion to measure the effect of explosion chamber dissipation. The multi-stage explosion chamber monitoring points are set before the first explosion chamber and after the last explosion chamber.

4. Analysis and Results of Experimental and Numerical Simulation

4.1. Wave Elimination Effect and Analysis in a Single-Stage Explosion Chamber

4.1.1. Study of the Straight Pipe Test

The peak shock wave overpressure represents the maximum damage pressure, establishing the peak shock wave overpressure suppression rate as $\alpha = \frac{P_1 - P_2}{P_1}$. The straight tube experiment controls the explosion chamber test, and Figure 11 depicts the peak shock wave overpressure versus time. The peak P1 sensor overpressure is 0.2738 MPa, and the peak P2 sensor overpressure is 0.3138 MPa. As a result, the peak shock wave overpressure suppression rate is $\alpha = -14.61\%$.

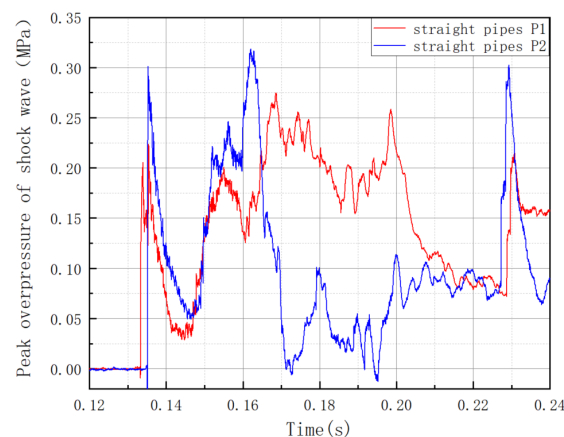


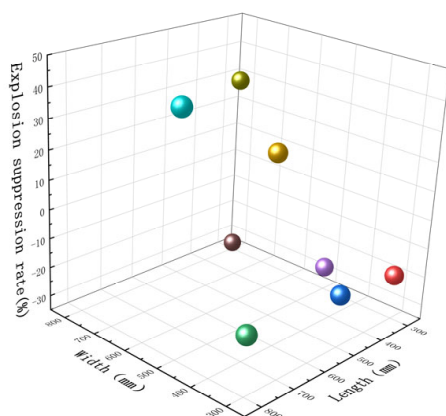
Figure 11. Relationship between shock wave overpressure and time in straight pipes.

4.1.2. Results of a Single-Stage Explosion Chamber Test

The shock wave rejection rates for various explosion chamber diameters are shown in Table 2. Figure 12 plots the shock wave rejection rate against the explosion chamber’s length and breadth. As shown in Table 2, the peak shock wave overpressure has been suppressed by the 5–5, 5–8, and 8–5 explosion chambers, while it has been augmented by the 3–3, 3–5, 3–8, 5–3, and 8–3 explosion chambers. According to our group’s previous research findings, the shock wave suppression rate is influenced by both the length and width of the explosion chamber. Table 2 and Figure 12 show that 5–5, 5–8, and 8–5 have strong shock wave suppression effects.

Table 2. Different-sized explosion chambers' inhibition rates.

Cavity Structure Size (Length × Width × Height)	Explosion Suppression Rate (α)
300 mm × 300 mm × 200 mm (3–3)	−19.55%
300 mm × 500 mm × 200 mm (3–5)	−16.91%
300 mm × 800 mm × 200 mm (3–8)	−14.69%
500 mm × 300 mm × 200 mm (5–3)	−26.91%
500 mm × 500 mm × 200 mm (5–5)	21.48%
500 mm × 800 mm × 200 mm (5–8)	45.27%
800 mm × 300 mm × 200 mm (8–3)	−32.60%
800 mm × 500 mm × 200 mm (8–5)	28.73%

**Figure 12.** Connection between explosion chamber length and breadth and shock wave suppression rate.

Shock waves are often suppressed at 21.48%, 45.27%, and 28.73% by 500 mm × 500 mm × 200 mm, 500 mm × 800 mm × 200 mm, and 800 mm × 500 mm × 200 mm diffusion chambers, respectively. Other-sized diffusion chambers also strengthen the shock wave. Utilizing a diffusion chamber that measures 500 mm × 500 mm × 200 mm by the size specifications of civil air defense engineering design is advised. The numerical simulation findings indicate that the formation of a reverse shock wave at the outflow is the principal method by which waves in a 500 mm × 500 mm × 200 mm diffusion chamber are attenuated. The reverse shock wave and the forward shock wave cancel each other to play a part in wave attenuation.

4.1.3. Analyzing the Dependability of Numerical Simulations

Error analysis is a crucial tool for the reliability analysis of numerical simulation, which confirms the reliability of numerical simulation by comparing the results of the numerical simulation with the results of the experiments, thereby providing a foundation for the more in-depth investigation of numerical simulation. The experimental data are discontinuous and unpredictable since different surroundings impact the explosion shock wave. Using the 55 explosion chamber as an example, a set of experimental data was chosen to calibrate the numerical simulation parameters, and several numerical simulation studies were carried out on this premise.

The explosion rapidly releases large amounts of energy and is more challenging to quantify. A 20% difference between the findings of the numerical simulation and the experiments is acceptable for engineering applications. As seen in Figure 13, which uses the peak shock wave overpressure at position P1 as an example, Figure 13a compares experimental and numerical simulation findings. The experimental result for P1 is 0.1611 MPa, whereas the numerical simulation result is 0.1573 MPa, resulting in a 3.42% error. Figure 13b compares the findings from experimental and numerical simulations of the peak shock wave

overpressure at position P2. The practical result for P2 is equivalent to 0.1525 MPa, whereas the result from the latter is 0.1489 MPa, resulting in a 2.36% error. The numerical simulation findings are regarded as credible since the error analysis reveals that the mistakes of the P1 and P2 measurement locations are less than 20%. Later, a more thorough investigation will be conducted using this numerical simulation parameter.

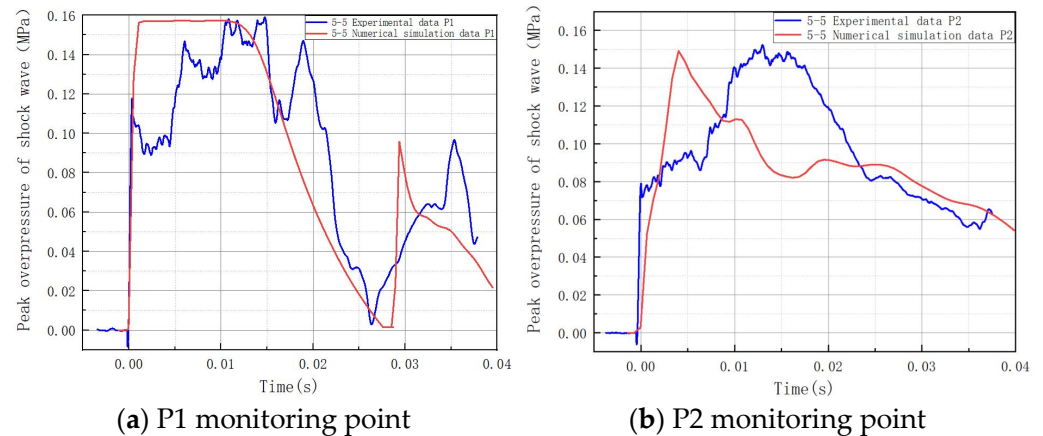


Figure 13. Comparison of simulations and experiments.

4.1.4. Study of the Single-Stage Explosion Chamber's Single-Stage Shock Wave Propagation Mechanism

Figure 14 depicts the explosion shock wave's progression through the 5–5 explosion chamber. Numerical simulations are used to examine the dissipation joints in the 5–5 explosion chamber. Figure 14 illustrates the division of the blast shock wave into the following processes as it propagates through the 5–5 explosion chamber:

- (1) Before entering the explosion chamber, the blast shock wave travels as a plane wave, as shown in Figure 14a.
- (2) The shock wave enters the explosion chamber as seen in Figure 14b, the cross-section abruptly rises, and the plane wave changes into a spherical wave.
- (3) As shown in Figure 14c, the spherical wave encounters the wall inside the explosion chamber and is reflected and superimposed. The high-pressure area of the shock wave is shifted to both sides of the explosion chamber, and a sparse wave is generated at the center of the explosion chamber structure. The shock wave is then reflected and superimposed on the wall inside the explosion chamber several times to form Mach reflection, resulting in the overpressure concern.
- (4) As seen in Figure 14d, when the shock wave propagates to the exit of the explosion chamber, the section suddenly decreases. The overpressure area on both sides of the wall inside the explosion chamber encounters the obstruction of the inner wall at the exit, causing the emission superposition again and weakening the shock wave. In contrast, the reflected shock wave with higher pressure gradually forms at the inner wall of the exit of the explosion chamber.
- (5) As seen in Figure 14e, the combined effect of the overpressure zone's reflection and superposition on both sides of the explosion chamber wall causes a reverse shock wave at the chamber's exit. The reverse shock wave and the forward shock wave cancel each other out, reducing the shock wave's energy.
- (6) The forward and backward shock waves cancel one another to generate a shock wave-canceling plane in the middle of the explosion chamber, as shown in Figure 14f.
- (7) As seen in Figure 14g, the combined impact of offset, reflection, and superposition considerably reduces the shock wave.

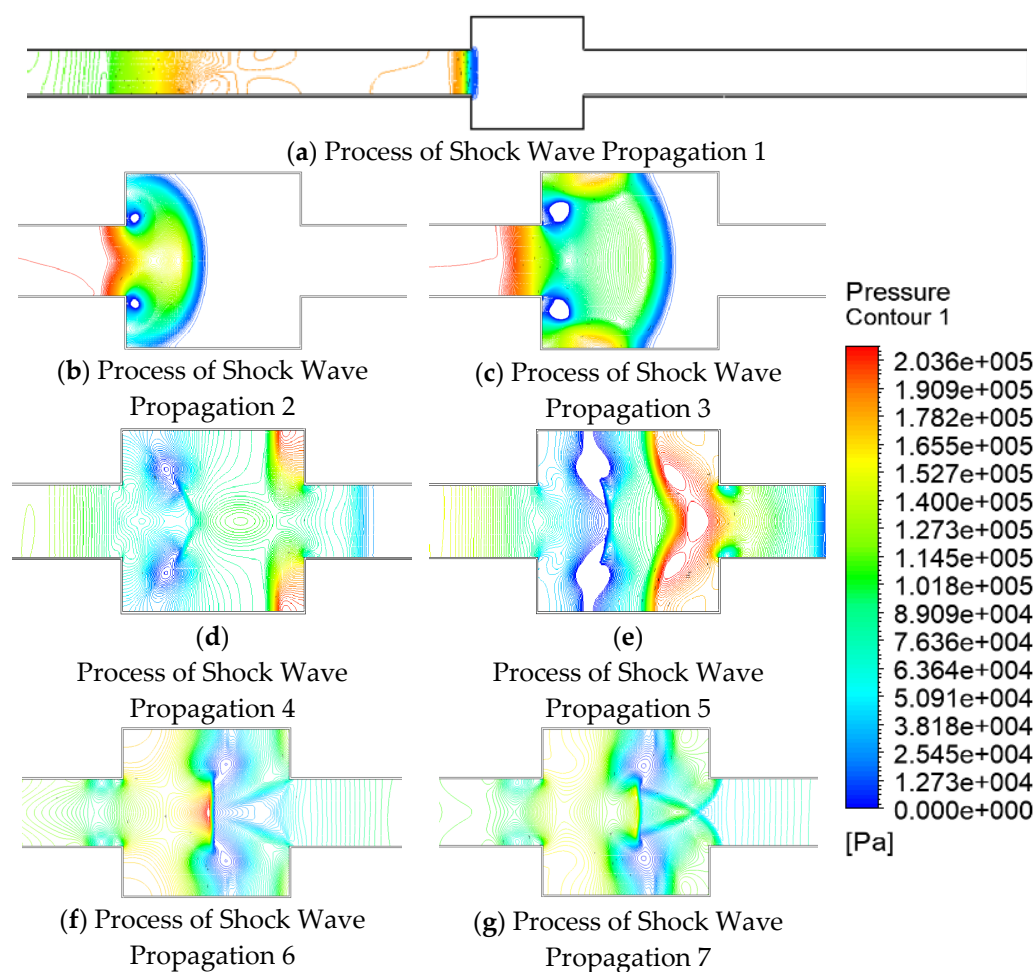


Figure 14. Explosion shock wave propagation in a 5–5 explosion chamber.

4.2. Wave Elimination Effect and Analysis for Multi-Stage Tandem Explosion Chambers

4.2.1. Results of Tests in a Multi-Stage Tandem Explosion Chamber

The test results for the multi-stage tandem explosion chamber are displayed in Figure 15. In the 55–35 two-section tandem explosion chamber depicted in Figure 15a, the peak overpressure at the P1 measurement point was 0.3278 MPa. The peak overpressure at the P2 measurement point was 0.1976 MPa, with an explosive suppression rate of 39.72%. The peak overpressure at the P1 measurement point is 0.2844 MPa, the peak overpressure at the P2 measurement point is 0.1326 MPa, and the explosion suppression rate is 53.37% for the 58–35–55 three-stage tandem explosion chamber depicted in Figure 15b. The 55 explosion chamber, for instance, has a peak overpressure suppression rate of 21.48%. Peak overpressure suppression rates increased for the 58–35–55 three-stage tandem explosion chamber by 31.89% compared to the 55 single-stage explosion chamber, the 58–35–35 two-stage tandem explosion chamber by 18.72% compared to the 55 single-stage explosion chamber, and the 55–35 two-stage tandem explosion chamber by 13.65% compared to the 55–35 two-stage tandem explosion chamber.

4.2.2. Multi-Stage Tandem Explosion Chamber Numerical Simulation Analysis

In total, 55 tandem two-, three-, four-, and five-segment explosion chambers were subjected to numerical simulations. Figure 16 displays the outcomes of measurement locations P1 and P2 in the numerical simulation. For the two-stage tandem explosion chamber, the shock wave overpressure suppression rate was 35.3176%; for the three-stage tandem explosion chamber, 43.337%; for the four-stage tandem explosion chamber, 43.199%; and for the five-stage tandem explosion chamber, 45.589%.

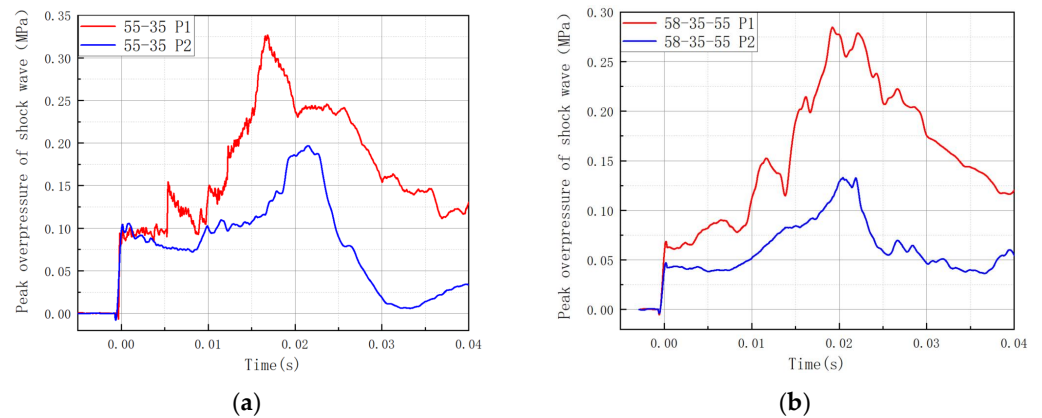


Figure 15. Multi-stage series explosion chamber test results. (a) Chamber with two-stage series diffusion (55–35); (b) chamber with three-stage series diffusion (58–35–55).

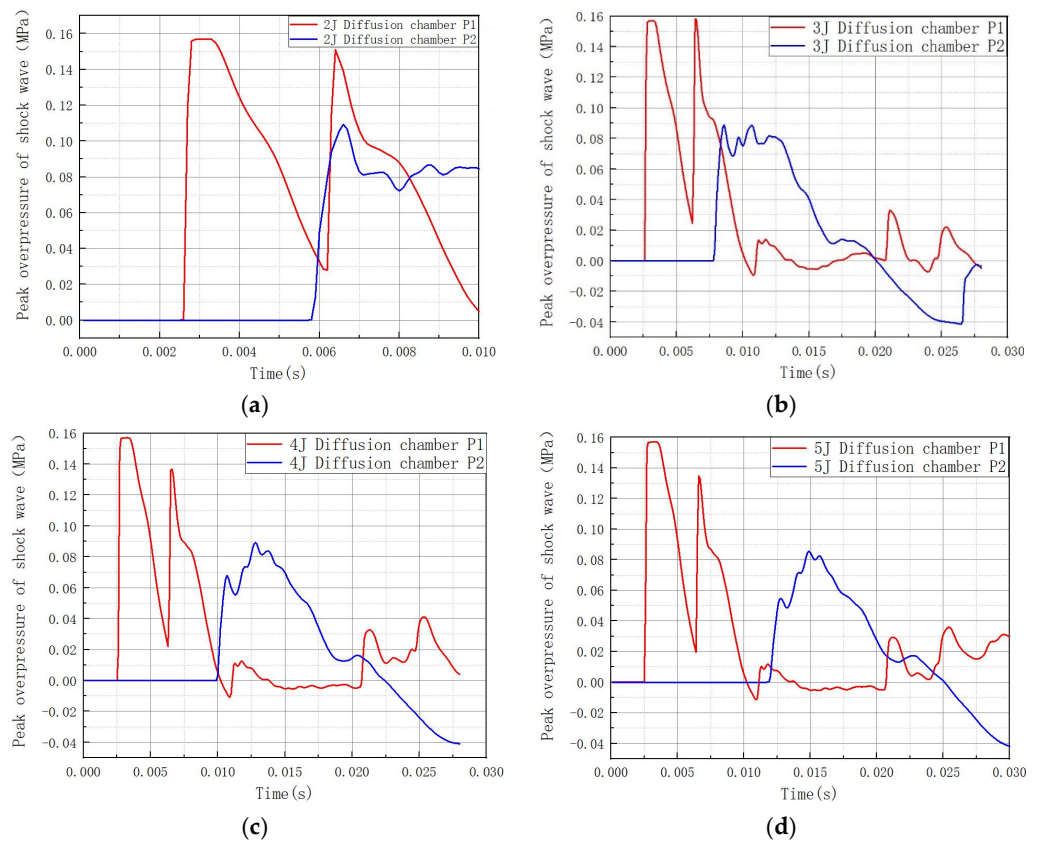


Figure 16. Results of multi-stage explosion chamber series connection from numerical simulation. (a) Chamber with two-stage series diffusion; (b) chamber with three-stage series diffusion; (c) chamber with four-stage series diffusion; (d) chamber with five-stage series diffusion.

The link between the shock wave overpressure rejection rate and the number of series stages is seen in Figure 17 and is stated as follows.

$$\alpha = e^{(3.8289 - 0.7988\beta^2)} \tag{7}$$

where α is the shock wave overpressure peak rejection rate, and β is the number of explosion chambers.

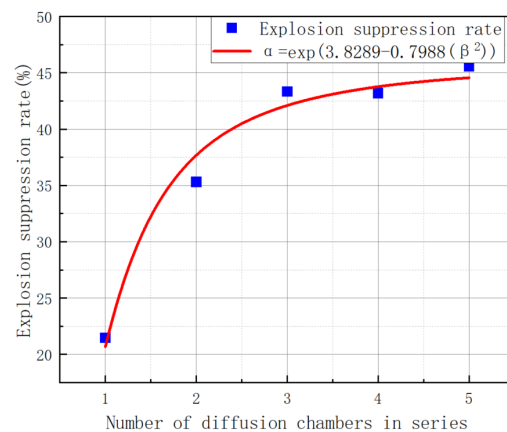


Figure 17. Connection between the number of series explosion chambers and the inhibition rate.

According to Figure 17, the shock wave overpressure peak suppression rate of the two-section tandem and three-section explosion chamber increases more quickly, indicating that they can produce a better wave elimination effect. The shock wave overpressure peak suppression rate of the four-section and five-section tandem explosion chambers changes less than that of the three-section.

Overall, it has been demonstrated through studies that the peak suppression rates of shock wave overpressure in the 58–35–55 three-stage series diffusion chamber and the 55–35 two-stage series diffusion chamber are both 39.72% and 53.37%, respectively. When compared to the 55 single-stage diffusion chamber, the 55–35 two-stage series diffusion chamber's overpressure peak suppression rate has increased by 18.72%. Comparing the 58–35–55 three-stage series diffusion chamber to the 55 single-stage diffusion chamber, the rate of overpressure peak suppression has increased by 31.89%. In comparison to the 55–35 two-stage series diffusion chamber, the overpressure peak suppression rate in the 58–35–55 three-stage series diffusion chamber is raised by 13.65%. The overpressure peak suppression rates in the second, third, fourth, and fifth stage diffusion chambers are 35.3176%, 43.3371%, 43.1995%, and 45.5897%, respectively, according to the numerical modeling of multi-stage series diffusion chambers based on 500 mm × 500 mm × 200 mm. Each diffusion chamber in a series has a propagation law for shock waves that is comparable to a single-stage diffusion chamber. The shock wave's energy has been greatly reduced by the time it reaches the fourth and fifth diffusion chambers, which causes the peak suppression rate of shock wave overpressure in the four- and five-section series diffusion chambers to rise more slowly. The shock wave's energy has been greatly reduced by the time it reaches the fourth and fifth diffusion chambers, which causes the peak suppression rate of shock wave overpressure in the four- and five-section series diffusion chambers to rise more slowly.

4.2.3. Study of the Multi-Stage Tandem Explosion Chamber's Shock Wave Propagation Mechanism

(1) Tandem explosion chamber with two sections

Figure 18 depicts the blast shock wave's progression inside the two-section tandem explosion chamber. As seen in Figure 18a, the shock wave enters the first explosion chamber and propagates as a spherical wave. It is reflected and superimposed as it strikes the explosion chamber wall, creating a high-pressure concentration zone. As seen in Figure 18b, a reverse shock wave develops at the inner wall of the shock wave exit, and the attenuated shock wave then enters the second explosion chamber. As illustrated in Figure 18c, the shock wave attenuated by the first explosion chamber enters the second explosion chamber, where the shock wave propagation mechanism is more like that of the first explosion chamber.

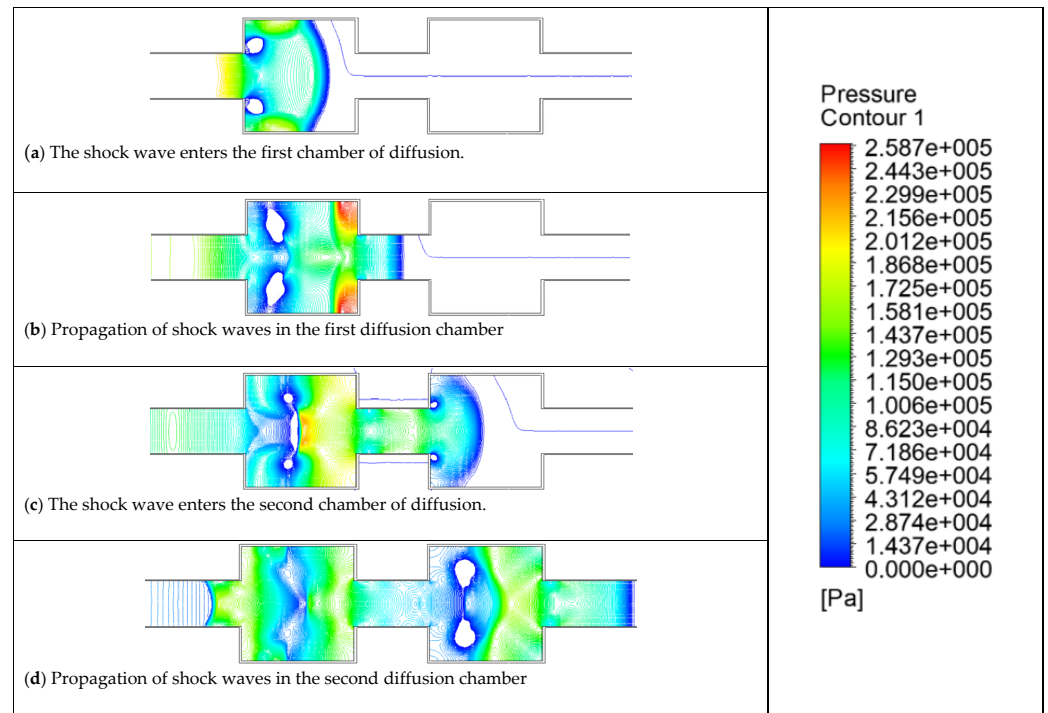


Figure 18. Process of a two-stage series explosion chamber’s shock wave propagation.

(2) Tandem explosion chamber with two sections

The shock wave’s progression through the multilayer explosion chamber is seen in Figure 19. Three-stage tandem explosion chambers are shown in Figure 19a, four-stage tandem explosion chambers are shown in Figure 19b, and a five-stage tandem explosion chamber is shown in Figure 19c. As illustrated in Figure 19, each single-stage explosion chamber inside the multi-stage tandem explosion chamber has a wave dissipation mechanism comparable to that of the single-stage cavity, and each portion of the explosion chamber can help dissipate the shock waves progressively. All subsequent diffusion chambers were unable to sufficiently attenuate the shock wave since the shock wave had already been greatly reduced by the first three diffusion chambers. Thus, employing a three-section explosion chamber structure is advised while building or renovating human defense projects.

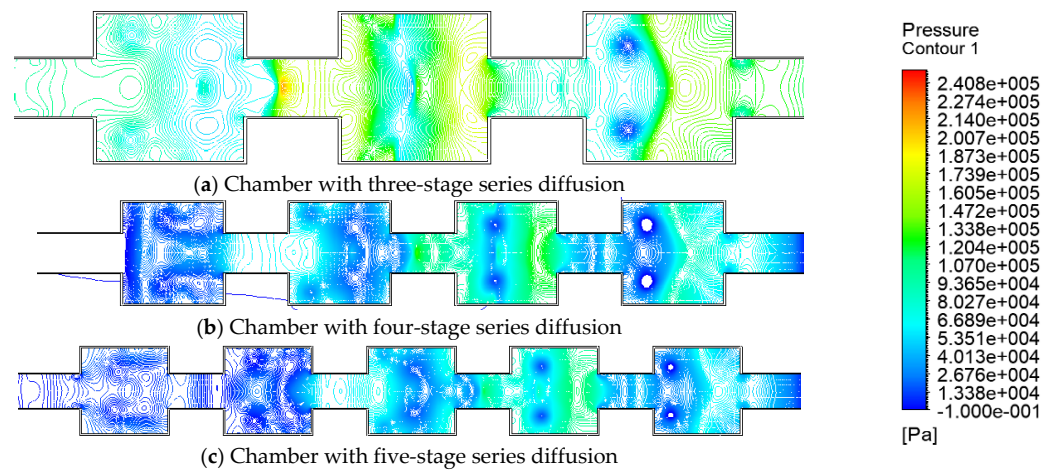


Figure 19. Process of a multi-stage series explosion chamber’s shock wave propagation.

4.3. Wave Elimination Effect and Study of Silencer-Type Explosion Chambers

4.3.1. Numerical Simulation Analysis of Silencer-Type Explosion Chamber

Due to building space restrictions, it is not possible to construct numerous explosion chambers in the restoration of existing human defense projects. As a result, the best possible design of the existing explosion chambers is crucial for enhancing the protection capacity. Since the silencer can cancel out sound waves, its structure serves as a guide for creating the explosion chamber’s ideal design. The outcomes of the numerical simulation of the explosion chamber for nine wave elimination plate angles are displayed in Figure 20. The link between the shock wave overpressure peak rejection rate and the wave elimination plate’s angle is seen in Figure 21. Figures 20 and 21 demonstrate that the wave elimination plate’s impact at 60° is the best, with an inhibition rate of 35.85%, while its effect at 90° is the poorest, with an inhibition rate of −5.45%. The various wave elimination plate angles significantly impact the rate of explosion suppression. The law is consistent with the form of the segmentation function. The fitting equations for the different curves were created by using the following equations to fit the parts:

$$\begin{cases} \alpha = 0.3981\theta + 11.8333, & \theta \leq 60^\circ \\ \alpha = -2.4339\theta + 181.8861, & 60^\circ < \theta \leq 75^\circ \\ \alpha = 0.2227\theta - 21.1774, & \theta > 75^\circ \end{cases} \quad (8)$$

where α is the shock wave overpressure peak rejection rate and θ is the wave elimination plate angle.

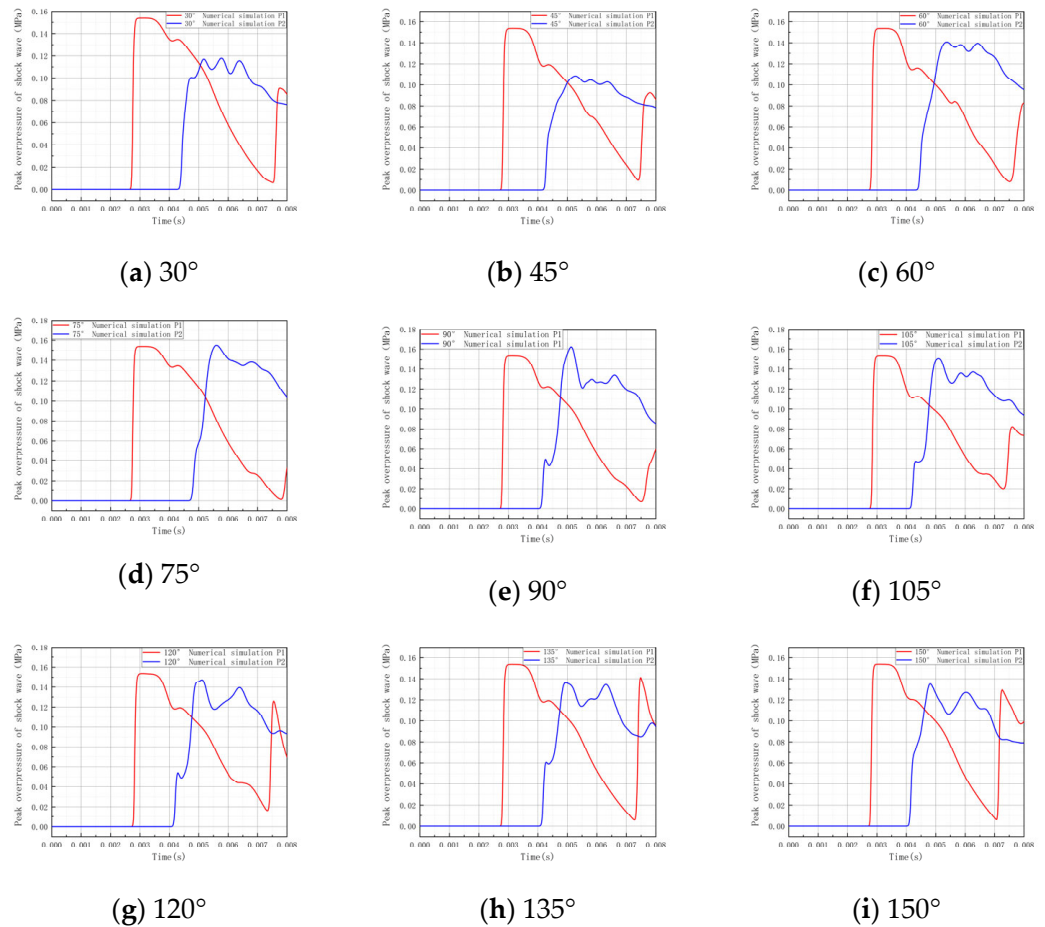


Figure 20. Results of numerical simulations of several explosion chambers of the muffler type.

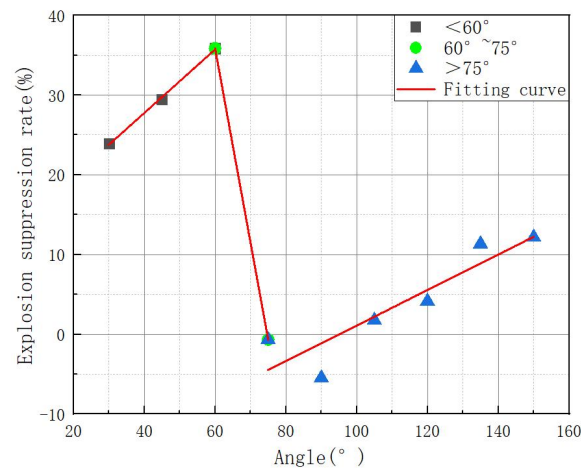


Figure 21. Connection between the angle of the shock wave damping plate and the peak suppression rate of the shock wave overpressure.

The silencing plate's angle significantly influences the explosion chamber's wave attenuation effect. The simulation results show that the 60° wave attenuation plate has the best wave attenuation effect, with a 14.37% increase over the original explosion chamber.

4.3.2. Study of Silencer-Type Explosion Chamber's Shock Wave Propagation Process

Figure 21 illustrates that the wave attenuation effect of a 60° muffler explosion chamber is the best, while a 90° muffler explosion chamber has the poorest wave attenuation effect. Hence, using the 60° and 90° explosion chambers as examples, the shock wave propagation process and the wave attenuation mechanism of the muffler-type explosion chamber are presented. Figure 22 illustrates how the explosion shock wave propagates after entering the explosion chamber at 60°. It passes through essentially the following stages:

- (1) As seen in Figure 22a, the shock wave from the explosion enters the explosion chamber and spreads as a spherical wave with an edge angle of about 60°.
- (2) As seen in Figure 22b, spherical waves hit the first set of the wave-absorbing plates' barrier and undergo reflection superposition, creating Mach reflection, an area of high pressure on one side of the wave-absorbing plate, and a reverse shock wave. Sparse waveforms in the center of the spherical wave when the shock waves are propagating forward and backward cancel each other out.
- (3) As seen in Figure 22c, whenever a spherical wave strikes a collection of wave-absorbing plates, it will reflect, stack, and create a region of high pressure at the wave-absorbing scale, creating a shock wave that reverses propagation and cancels out the shock wave that propagates forward. The cross-section suddenly shrinks when the shock wave reaches the explosion chamber's outlet. The overpressure zones on both sides of the chamber wall collide with the inner wall barrier at the outlet, causing the emission superposition to happen once more and the shock wave to weaken again.
- (4) As seen in Figure 22d, the inner wall at the explosion chamber's outflow produces a high-pressure reverse shock wave. As the reverse shock wave hits the obstruction on the other side of the muffler plate, it is reflected and superimposed again, causing the shock wave to lose strength at the corner where it exits progressively.
- (5) As seen in Figure 22e, the shock wave experiences complicated emission superposition at the exit to create a reverse shock wave. This reverse shock wave cancels out the front shock wave, causing the shock wave to dwindle progressively.
- (6) The energy of the backward propagating shock wave is rather considerable, as seen in Figure 22e. The reverse shock wave continues to move in the opposite direction after the forward shock wave cancels it out, creating a sparse wave at the outlet. The

complicated cancellation, reflection, and superposition caused by the muffler plate and explosion chamber significantly weaken the shock wave.

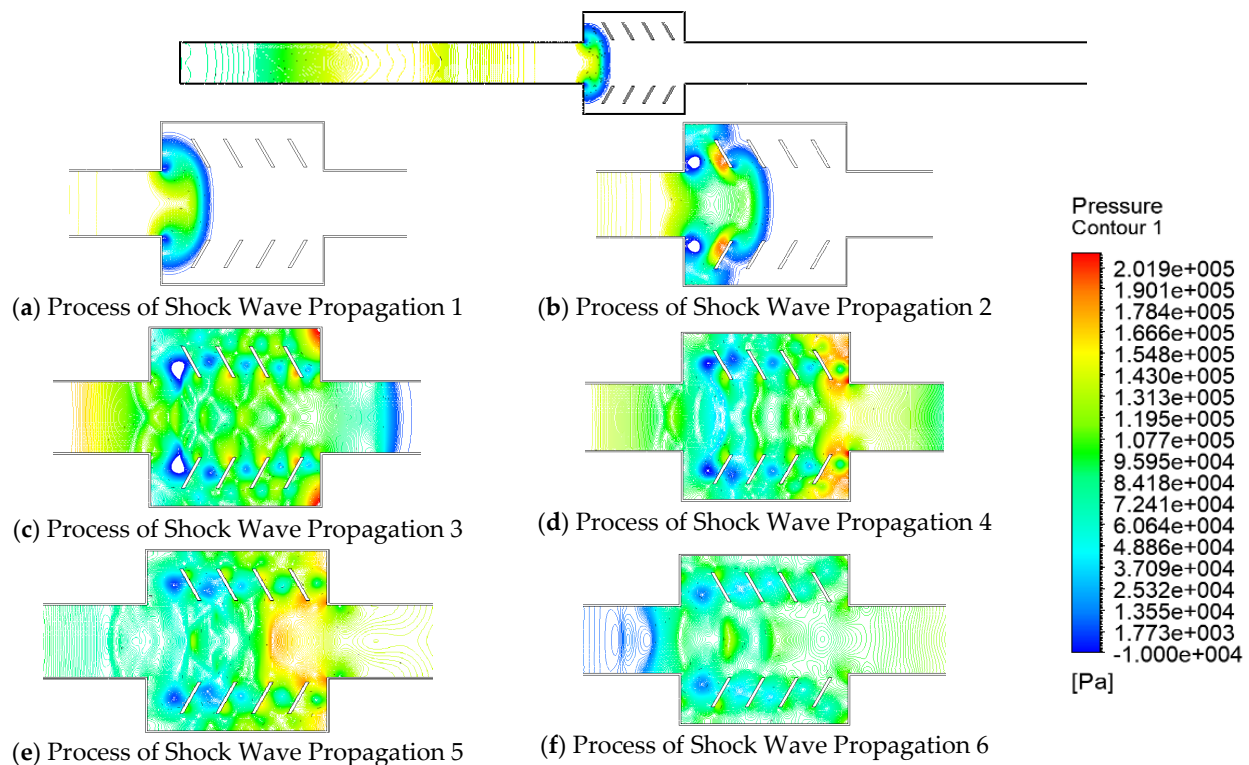


Figure 22. Process of shock wave propagation in a 60° muffler explosion chamber.

According to Figure 23, the explosion shock wave propagates via the following stages after entering the 90° muffler explosion chamber:

- (1) As seen in Figure 23a, once the shock wave enters the explosion chamber as a spherical wave, it collides with the wave-absorbing plate, creating a region of high pressure and energy in which an overpressure concentration occurs.
- (2) As seen in Figure 23b, a sparse wave is created in the explosion chamber's center, and the spherical wave and reverse shock wave combine to form Mach reflections in the complex reflection superposition. This causes several high-pressure concentration areas on the explosion chamber wall and causes the wave to propagate forward.
- (3) As seen in Figure 23c, the cross-section rapidly contracts, and, at the exit, the overpressure zones on each side of the explosion chamber wall come together with the inner wall's barrier to produce a high-pressure concentration zone. In the small area created by the muffler plate and the explosion chamber wall, the shock wave experiences complicated emission superposition to create Mach reflection, progressively propagating towards the explosion chamber outlet.
- (4) As seen in Figure 23d, when shock waves from both sides congregate at the explosion chamber's exit, they are obstructed by the edges of the silencing plate. After complicated emission stacking takes place, a forward shock wave is created.
- (5) The superposition of two forward shock waves creates an overpressure concentration zone at the outflow, as seen in Figure 23e.
- (6) As seen in Figure 23f, the forward propagating shock wave forms a spherical wave at the exit and continues to propagate, and the inner wall once more attenuates the shock wave. Positive shock waves are created at the door due to the simultaneous action of the explosion chamber structure and muffler plate, which has a poor attenuating impact on the waves.

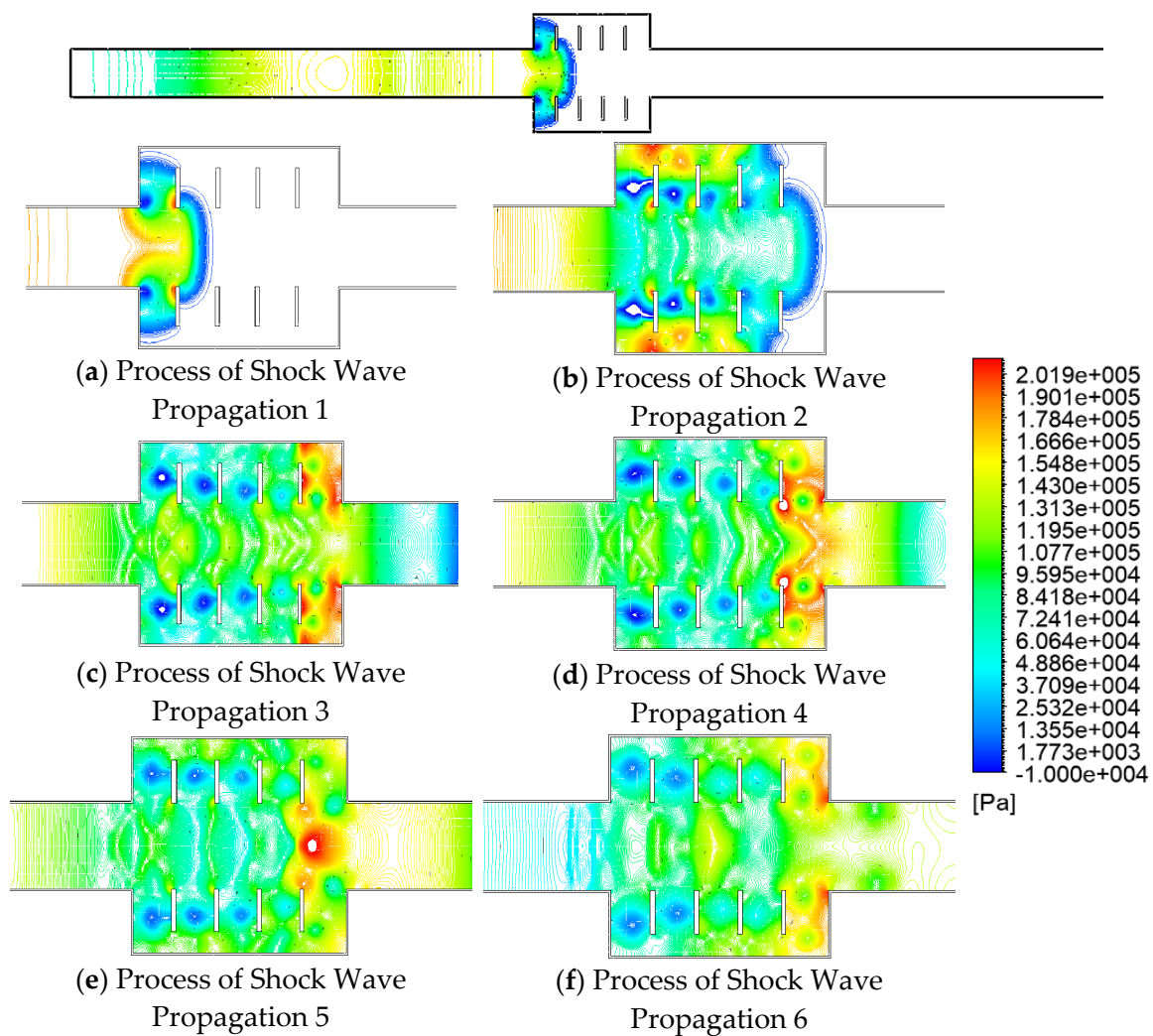


Figure 23. Process of shock wave propagation in a 90° muffler explosion chamber.

Figure 24 depicts the shock wave propagation mechanism in an explosion chamber at 30°, 45°, 75°, 105°, 120°, 135° and 150°. The wave attenuation process in the 30° and 45° explosion chambers is comparable to that in the 60° explosion chamber, and the wave attenuation result is good in both. The 105°, 120°, 135°, and 150° explosion chambers have low wave attenuation effects, and the wave propagation mechanism is comparable to that of the 90° explosion chamber. Two primary factors, in general, influence how wave attenuation works:

- (1) The wave attenuation effect of 30°, 45°, and 60° sound attenuation plates is good because they can direct the shock wave at the exit to generate a reverse shock wave, which can cancel out the original shock wave. A positive shock wave is created at the outlet of the sound attenuation plates of 75°, 90°, 105°, 120°, 135°, and 150° to some extent. This positive shock wave is superimposed on the initial positive shock wave and increases its power, resulting in inadequate wave attenuation.
- (2) The impact results in the formation of overpressure concentration zones on both sides of the explosion chamber wall due to the silencing plates at 75°, 90°, 105°, 120°, 135°, and 150°. After coming into contact with the outlet's inner wall's barrier and going through a complicated reflection superposition, the overpressure concentration zone keeps moving ahead and eventually becomes a high-energy shock wave. Positive shock waves are less likely to arise when silencing plates with 30°, 45°, and 60° angles are used to prevent the development of high-energy overpressure concentration zones on each side of the explosion chamber wall.

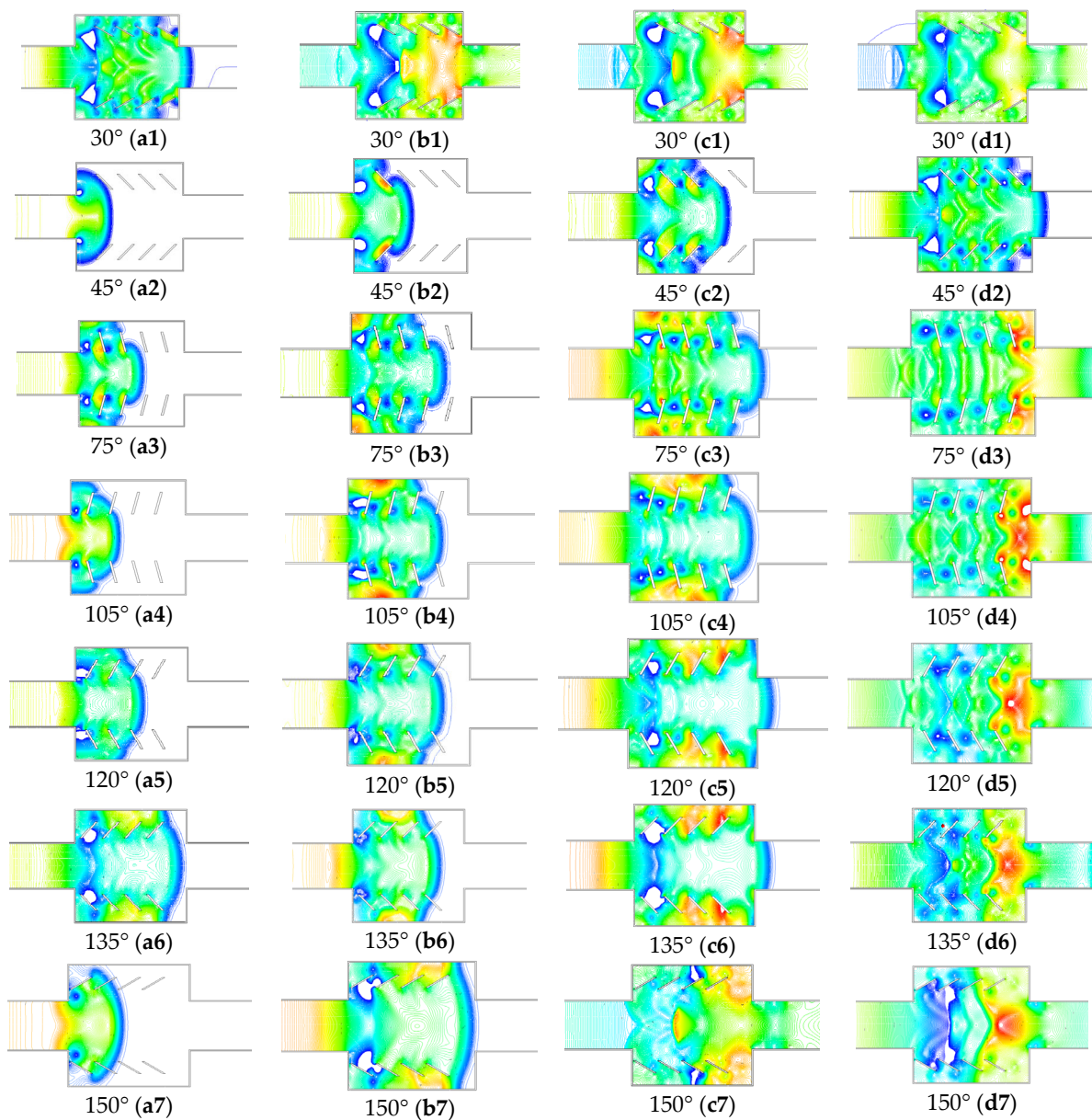


Figure 24. Process of shock wave propagation in an explosion chamber of the multi-angle muffler type.

In conclusion, numerical simulations of muffler-type diffusion chambers at various angles reveal that the 30°, 45°, and 60° muffler diffusion chambers exhibit better wave attenuation effects, whereas the 75°, 90°, 105°, 120°, 135°, and 150° muffler diffusion chambers exhibit poorer wave attenuation effects. The best wave attenuation among them is achieved by the 60° muffler diffusion chamber, while the maximum wave attenuation is achieved by the 90° muffler diffusion chamber. The shock wave overpressure is suppressed to a maximum of 35.85% in the 60° muffler diffusion chamber and to a maximum of −5.45% in the 90° muffler diffusion chamber. A piecewise function describes the link between the angle of the silencing plates and the rate of explosion suppression. The 30°, 45°, and 60° muffler diffusion chambers go through complex reflection and superposition to create reverse shock waves, which cancel out each other with forward shock waves to produce a good wave attenuation effect, according to the analysis of the shock wave propagation process.

5. Conclusions

This article examines the propagation law and procedure of shock waves in various diffusion chambers, estimates the wave attenuation impact of different diffusion chamber types using numerical simulations and experimentation, and describes the ideal diffusion chamber size and style. The following are the primary conclusions:

- (1) The diffusion chamber with dimensions of 500 mm × 500 mm × 200 mm effectively weakens shock waves. It uses a complicated reflection superposition technique to attenuate waves, creating a reverse shock wave at the exit. The role of the reverse and forward shock waves is to cancel one another and attenuate the wave.
- (2) The suppression rate of the overpressure peak increased in the 55–35 series diffusion chamber by 18.72% compared to the 55 single-stage diffusion chamber, in the 58–35–55 three-stage series diffusion chamber by 31.89%, and in the 58–35–55 three-stage series diffusion chamber by 13.65% compared to the 55–35 two-stage series diffusion chamber.
- (3) After passing through a three-stage series diffusion chamber, the shock wave's peak overpressure was dramatically lowered. Considering the building size and cost, it is advised to employ a three-stage series diffusion chamber in civil air defense engineering construction.
- (4) Analysis of the shock wave propagation mechanism shows that the complicated reflection and superposition in the 30°, 45°, and 60° muffler diffusion chambers create reverse shock waves, which cancel out forward shock waves and have an excellent attenuating effect. Therefore, it is advised to utilize a 60° muffler diffusion chamber to remodel civil air defense engineering.

Author Contributions: Conceptualization, X.X. and W.L.; methodology, W.L.; software, W.L.; validation, H.Y., X.X. and W.L.; formal analysis, X.X.; investigation, H.Y.; resources, H.Y. and L.Z.; data curation, W.L.; writing—original draft preparation, W.L. And X.X.; writing—review and editing, H.Y. and W.L.; visualization, W.L.; supervision, H.Y.; project administration, H.Y. and W.L.; funding acquisition, H.Y. and L.Z. All authors have read and agreed to the published version of the manuscript.

Funding: This research was funded by the Postgraduate Research & Practice Innovation Program of Jiangsu Province (KYCX22_0682).

Informed Consent Statement: Written informed consent has been obtained from the patient(s) to publish this paper.

Data Availability Statement: Not applicable.

Acknowledgments: We appreciate the technical support from the 'State Key Laboratory of Mining Response and Disaster Prevention and Control in Deep Coal Mines, Anhui University of Science and Technology'. The above content has been approved by all of our authors.

Conflicts of Interest: The authors declare no conflict of interest.

References

1. Liu, W.; Xu, X.; Mu, C. Experimental Study on Two-Phase Explosion Suppression of Gas/Pulverized Coal by Explosion Suppressant. *ACS Omega* **2022**, *7*, 16644–16652. [[CrossRef](#)] [[PubMed](#)]
2. Peng, Z.; Zanganeh, J.; Moghtaderi, B. Influence of Gradually Inflated Obstructions on Flame Propagation in a Tube Closed at One End. *Fire* **2023**, *6*, 154. [[CrossRef](#)]
3. Bosikov, I.I.; Martyushev, N.V.; Klyuev, R.V.; Savchenko, I.A.; Kukartsev, V.V.; Kukartsev, V.A.; Tynchenko, Y.A. Modeling and Complex Analysis of the Topology Parameters of Ventilation Networks When Ensuring Fire Safety While Developing Coal and Gas Deposits. *Fire* **2023**, *6*, 95. [[CrossRef](#)]
4. Chen, S.; Liu, W.; Mu, C. Research on the Rule of Explosion Shock Wave Propagation in Multi-Stage Cavity Energy-Absorbing Structures. *Materials* **2023**, *16*, 4608. [[CrossRef](#)] [[PubMed](#)]
5. Liu, W.; Mu, C.; Li, Z. Influence of cavity structure on gas explosion characteristics in coal mine. *Powder Technol.* **2022**, *398*, 117084. [[CrossRef](#)]

6. Shi C, Z.J.W.X. Improving the Impact Resistance and Antisplash of Civil Air Defense Wall: Experiments and Finite-Element Simulation. *J. Struct. Eng.* **2023**, *2*, 4022238. [[CrossRef](#)]
7. Iqbal, N.; Sharma, P.K.; Kumar, D.; Roy, P.K. Protective polyurea coatings for enhanced blast survivability of concrete. *Constr. Build. Mater.* **2018**, *175*, 682–690. [[CrossRef](#)]
8. Bivol, G.; Golovastov, S. Effects of polyurethane foam on the detonation propagation in stoichiometric hydrogen-air mixture. *Process Saf. Environ.* **2019**, *130*, 14–21. [[CrossRef](#)]
9. Luo, Z.; Su, Y.; Chen, X.; Zheng, L. Effect of BC powder on hydrogen/methane/air premixed gas deflagration. *Fuel* **2019**, *257*, 116095. [[CrossRef](#)]
10. Zhao, Q.; Chen, X.; Yang, M.; Zhang, H.; Huang, C.; Dai, H.; Li, Y.; Liu, J.; Zhu, H. Suppression characteristics and mechanisms of ABC powder on methane/coal dust compound deflagration. *Fuel* **2021**, *298*, 120831. [[CrossRef](#)]
11. Li, M.; Xu, J.; Li, Q.; Wang, C.; Wang, B.; Jiang, J. Explosion mitigation of methane-air mixture in combined application of inert gas and ABC dry powders in a closed compartment. *Process Saf. Prog.* **2020**, *39*, e12101. [[CrossRef](#)]
12. Song, Y.; Zhang, Q. The quantitative studies on gas explosion suppression by an inert rock dust deposit. *J. Hazard. Mater.* **2018**, *353*, 62–69. [[CrossRef](#)] [[PubMed](#)]
13. Fan, R.; Jiang, Y.; Li, W.; Xiong, C.; Qiu, R. Investigation of the physical and chemical effects of fire suppression powder NaHCO_3 addition on methane-air flames. *Fuel* **2019**, *257*, 116048. [[CrossRef](#)]
14. Liu, T.; Yin, X.; Liu, Y.; Tang, Y.; Huang, A.; Dong, X.; Liu, Y. Influence of Water Mist Temperature Approach on Fire Extinguishing Effect of Different Pool Fires. *Processes* **2022**, *10*, 1549. [[CrossRef](#)]
15. Pei, B.; Li, J.; Wang, Y.; Wen, X.; Yu, M.; Jing, G. Synergistic inhibition effect on methane/air explosions by N_2 -twin-fluid water mist containing sodium chloride additive. *Fuel* **2019**, *253*, 361–368. [[CrossRef](#)]
16. Cao, X.; Wang, Z.; Lu, Y.; Wang, Y. Numerical simulation of methane explosion suppression by ultrafine water mist in a confined space. *Tunn. Undergr. Sp. Tech.* **2021**, *109*, 103777. [[CrossRef](#)]
17. Lu, C.; Wang, H.; Pan, R.; Zhang, Y.; Yu, M. Preventing the propagation of gas explosion in ducts using spurted nitrogen. *Process Saf. Environ.* **2019**, *123*, 11–23. [[CrossRef](#)]
18. Jiang, B.; Liu, Z.; Tang, M.; Yang, K.; Lv, P.; Lin, B. Active suppression of premixed methane/air explosion propagation by non-premixed suppressant with nitrogen and ABC powder in a semi-confined duct. *J. Nat. Gas Sci. Eng.* **2016**, *29*, 141–149. [[CrossRef](#)]
19. Yang, K.; Zhang, P.; Yue, C.; Chen, K.; Ji, H.; Xing, Z.; Hao, Y.; Jiang, J. Experimental research on methane/air explosion inhibition using ultrafine water mist containing methane oxidizing bacteria. *J. Loss Prevent. Proc.* **2020**, *67*, 104256. [[CrossRef](#)]
20. Wang, Y.; Ma, H.; Han, L.; Xu, X.; Skrzykowski, K.; Bascompta, M. Mechanism Analysis of Airbag Explosion Suppression and Energy Absorption in a Flexible Explosion Suppression System. *Fire* **2023**, *6*, 224. [[CrossRef](#)]

Disclaimer/Publisher's Note: The statements, opinions and data contained in all publications are solely those of the individual author(s) and contributor(s) and not of MDPI and/or the editor(s). MDPI and/or the editor(s) disclaim responsibility for any injury to people or property resulting from any ideas, methods, instructions or products referred to in the content.